

Analysis of Soil Pressure Distribution and Fracture Surface Inside Mechanically Stabilized Earth (MSE) Walls of High-Speed Railways

Guangpeng Liu^{1,2,3,*}, Nan Zhang^{2,3}, Guoliang Shi^{2,3}, Weiming Huang^{2,3} and Hong Xiao⁴

¹*School of Civil Engineering, Sun Yat-sen University, Guangzhou 510275, China*

²*Guangzhou Construction Group Co., Ltd, Guangzhou 510030, China*

³*Guangzhou Municipal Group Design Institute Co., Ltd, Guangzhou 510060, China*

⁴*School of Civil Engineering, Beijing Jiaotong University, Beijing 100044, China*

Keywords: MSE Wall, Model Test, Soil Pressure, High-Speed Railway, Fracture Surface.

Abstract: Due to the extremely strict settlement requirements for the high-speed railways, the MSE wall, as an environmentally friendly structure, the variation of the soil pressure and the fracture surface are related to the accurate design of the wall. Three sets of model tests were designed based on the similar theory, and the soil pressure changes in the MSE wall and the retaining wall panel under different loads were studied respectively. At the same time, the high-speed train-track-MSE wall model was conducted to analyze the dynamic loading effect, the distribution of soil pressure and the changes of fracture surface. The result shows that: increasing the layers of ribs and increasing the length of ribs will reduce the soil pressure. Under static load, the soil pressure inside the MSE wall increases linearly along the wall height, while under the train load, the soil pressure increases linearly in the stable area and increases non-linearly in the active area. In the designing, the fracture surface of the MSE wall is considered to be a fixed value. However, if the failure of the ribs in the range of 0.15H~0.25H at the bottom of the wall occurs, the position of the fracture surface will move upward along the wall. The guidelines suggest when designing the high-speed rail MSE walls, 0.15H~0.25H range should be strengthened.


1 INTRODUCTION

MSE wall is composed of reinforcement ribs, wall panels, and connecting parts. Due to its outstanding advantages such as less land occupation, low cost, and easy construction, it has been widely used in railway infrastructure.

Many scholars have also conducted a large amount of theoretical and experimental research. Jean et al. (Jiang et al., 2016; Noike et al., 2004; Jean et al., 2015; Alain et al., 2017) combined full-scale model tests with finite element simulation calculations to simulate train loads using harmonic loads, and calculated the mechanical characteristics of MSE walls. Fei et al. (2018) used a combination of centrifugal testing and finite element strength reduction method to study the fracture surface forms of MSE walls with different step forms. Ehsan et al. (2018) regarded the MSE wall as a two-phase medium material and calculated the form of the

fracture surface. Mohammad et al. (2018) used a combination of experimental and numerical simulation methods to study the deformation and soil pressure changes of MSE walls under different external loads.

Xiao et al. (2021) monitored the horizontal displacement, soil pressure, and potential sliding surface of the wall through large-scale indoor model tests of a two-step MSE wall, and analyzed the evolution law of the stepped MSE wall fracture surface. Wang et al. (2023) conducted indoor model tests to analyze the changes in mechanical behavior of MSE walls, such as settlement, horizontal displacement of panels, lateral soil pressure coefficient, and grid strain. Ren et al. (2021) conducted indoor model tests on MSE walls under horizontal static dynamic loads, exploring the deformation, horizontal soil pressure, reinforcement strain, and potential fracture surface of the retaining walls. Xu et al. (2023) used model calculations to

 <https://orcid.org/0000-0002-3711-7902>

study the variation law of the bearing capacity of retaining walls under strip loads. Yang et al. (2021) analyzed the evolution law of vertical stress, geogrid strain, and settlement of the foundation and wall during construction and after construction through on-site in-situ tests of railway retaining walls.

From the above research, it can be seen that most scholars currently focus on static load testing and theoretical research, while some scholars mainly use harmonic loads to replace train loads. However, there is no specific design for MSE walls for high-speed railways in the existing railway design rules. In order to further study the soil pressure, fracture surface changes, and stability characteristics of MSE walls for high-speed railways under static and dynamic loads, a model test of the retaining wall was first carried out. Then, a dynamic coupling model of the MSE wall for high-speed railways was established based on finite element analysis. The changes in soil pressure and reinforcement stress of the retaining wall under vehicle loads were calculated. Based on the failure of reinforcement materials, the change law of the fracture surface inside the retaining wall was calculated. Relevant research can provide data support for the accurate designing of MSE walls for high-speed railways in the future.

2 MODEL TEST

2.1 Experimental

The experiment in this article is based on an intercity railway MSE wall. The MSE wall has a height of 7.8m, and the wall panels are made of C30 concrete with a size of $0.5m \times 0.3m \times 0.3m$. The geogrid is unidirectional made of high-density polyethylene material, whose length is $8.0 \sim 10.5m$.

2.2 Model Similarity Relationship

The similarity theorem (Du et al., 2018; TB 10621-2014) was used to calculate the model geometric similarity, and the geometric similarity constant $C_l=10$, strain similarity constant $C_\epsilon=1/10$, soil density similarity ratio $C_\rho=1$, soil elastic modulus similarity $C_E=1$, and tensile modulus similarity constant of the reinforcement $C_{El}=10$. According to the similarity π law, the similarity relationship of

the other parameters is calculated as follows: stress similarity ratio $C_\sigma = C_\gamma C_l = 1$, bulk density similarity ratio $C_\gamma = 1/10$, and Poisson's ratio similarity $C_\mu = 1$.

2.3 Similar Materials

The model experiment takes sand as the filler, with an optimal moisture content 11%, compaction degree 0.94, and dry density $1.85g/cm^3$. When the optimal moisture content is reached, the density of sand is $2.04g/cm^3$.

The wall adopts modular facing panels, considering the convenience of production and assembly. In the experiment, wood panels can meet the relevant requirements.

This model experiment uses a unidirectional tensile geogrid as the ribs, with a nominal tensile strength $\geq 25kN/m$. Other physical and mechanical properties are shown in Table 1.

2.4 Test Design

Three sides of the model box are made of 1.5cm thick tempered glass, and the wall is composed of a wooden board with dimensions $5cm \times 3cm \times 3cm$ (length 5cm width 3cm height 3cm) connected as a whole using steels. Set up horizontal barriers at the bottom of the wall to simulate the limiting effect of the foundation on the wall bottom.

The size of the model box is determined by the geometric similarity relationship (length x width x height), with a filling height of 0.78m. It is filled in layers and compacted.

Set up a plate in the middle of the wall and use a pressure sensor to control the jack to accurately loading. According to the railway design specifications, the maximum designing load on the top of the track foundation is 54.1kPa. At the same time, in order to study the variation of the wall under different loads, step-by-step loading is adopted.

When using a jack for loading in the experiment, the magnitude of the applied load is determined through a pressure sensor, and the magnitude and variation of the loading force are recorded and controlled through an IMC data acquisition instrument. The method of burying soil pressure boxes inside the wall is adopted to measure the soil pressure. The test site is shown in Figure 1.

Table 1: Geogrid physical parameters.

nominal tensile strength (kN/m)	elongation at yield (%)	Tensile force at 2% elongation (kN/m)	Tensile strength at 5% elongation (kN/m)	The spacing between individual tendons(mm)	Thickness of single rib (mm)
≥ 25	≤ 10	≥ 7	≥ 14	30	1



Figure 1: Test model.

Due to the fact that the spacing and length of ribs are the main factors in the design of MSE walls (Yang, 2015), three sets of different spacing and length of ribs were tested under different cases. The spacing and length of ribs in each set of tests are shown in Table 2.

Table 2: Test case.

case	Number of ribs layers	ribs spacing /m	ribs length /m
1	7	0.1	0.8
2	5	0.15	0.8
3	5	0.15	1

3 RESULTS AND DISCUSSION

3.1 Soil Pressure on Retaining Wall

Under static load, tests were conducted on the horizontal soil pressure of MSE walls at different heights. The comparison of horizontal soil pressure on the walls with different ribs layers is shown in Figure 2(a), and the comparison of soil pressure with different ribs lengths is shown in Figure 2(b).

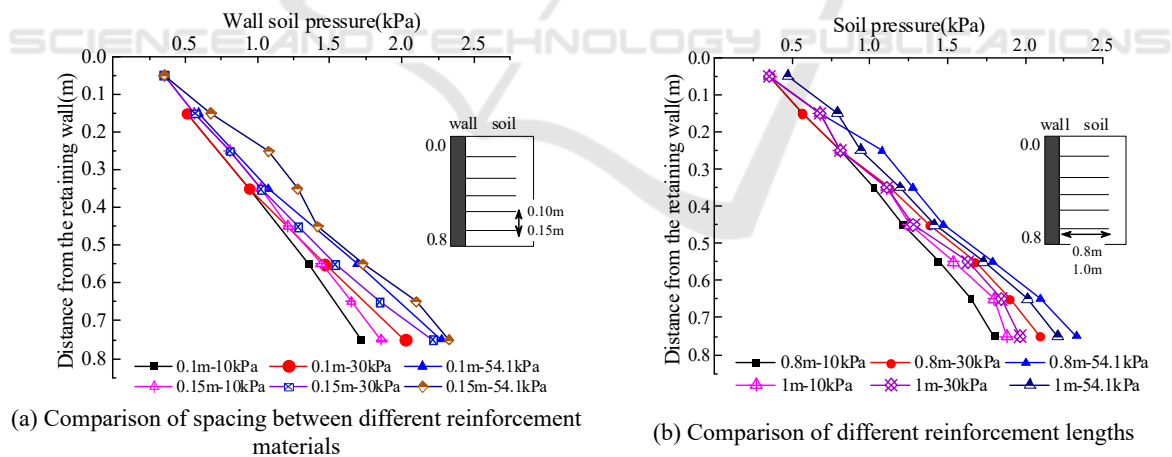


Figure 2: Distribution of soil pressure with burial depth under static load.

Overall, the horizontal soil pressure on the wall shows a non-linear and gradually increasing trend in the vertical direction. From the different spacing of ribs in Figure 2(a), it can be seen that the soil pressure in case 2 is higher than that in case 1, indicating that increasing the number of ribs layers and reducing the vertical spacing of ribs can effectively reduce the distribution of soil pressure.

From Figure 2(b), it can be seen that overall, the soil pressure at the bottom under case 2 is higher than that under case 3, indicating that increasing the length of the ribs can effectively reduce the distribution of soil pressure.

3.2 Vertical Soil Pressure inside the MSE Wall

In the case where the number of ribs layers is the same and all ribs are buried in the same position, the influence of different ribs lengths on the vertical soil pressure inside the was studied. The comparison of experimental data for conditions 2 and 3 is shown in Figure 3.

Under static load, the vertical soil pressure inside the wall exhibits a non-linear distribution along the length of the ribs, with the maximum soil pressure occurring near the loading position and smaller at ends. This is mainly because near the wall, due to the horizontal displacement of the wall, soil pressure near the wall is released. The soil on the side far away from the load position is less affected by external loads.

From Figure 3(a), it can be seen that the length of the ribs has a significant impact on the soil pressure

at the bottom of the wall. The soil pressure in case 2 is significantly higher than that in case 3. The ribs increased from 0.8m to 1m, and the maximum soil pressure at the bottom decreased by an average of 0.25KPa, about 1.4%. In Figure 3(b), the maximum soil pressure at the bottom end decreased by an average of 0.17 KPa, approximately 1.1%. In Figure 3 the maximum soil pressure at the bottom decreased by an average of 0.08KPa, approximately 0.5%. The length of the ribs in Figure 3 has little effect on the soil pressure value at the top of the wall. The influence of the length of the ribs on the soil pressure inside the wall gradually weakens from the bottom to the top.

To analyze the variation of soil pressure along the height of the wall, the data of soil pressure along the height of the wall at distances of 0.07m, 0.32m, 0.57m, 0.82m, and 1.07m are shown in Figure 4.

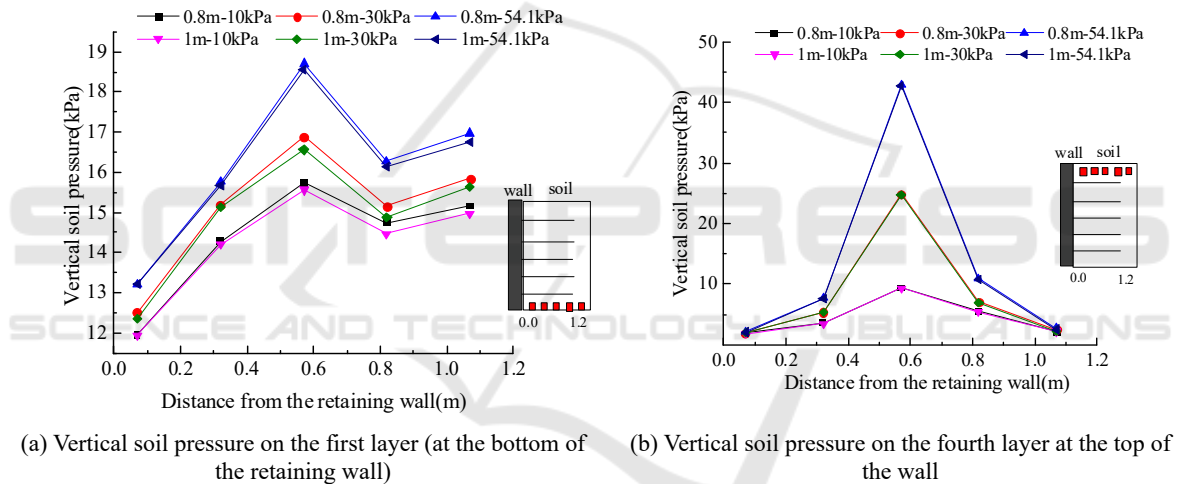


Figure 3: Distribution of vertical soil pressure along the reinforcement under static load.

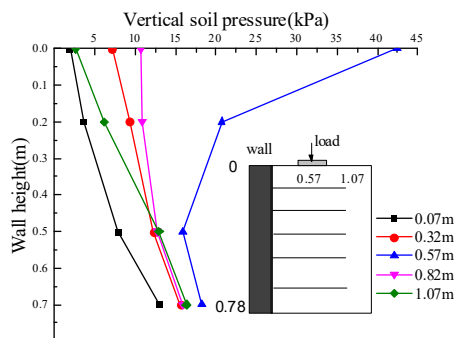


Figure 4: Distribution of vertical soil pressure inside the retaining wall under static load.

From the Figure 4, it can be concluded that except for the 0.57m below the loading position, the soil pressure inside the wall at all other positions increases linearly with the height, which is basically consistent with the law described by Coulomb's soil pressure. At a height of 0.57m, the soil pressure inside the wall shows a non-linear trend. This is mainly due to the energy dissipation of the soil below the wall under external forces, which continuously decreases along the depth of the wall. At the same time, there is a certain increasing trend at the bottom of the wall, which is because the bottom of the wall is outside the range of external load influence.

4 NUMERICAL SIMULATION

4.1 Modeling

The subgrade in the model adopts the Mohr Coulomb constitutive model, and the embedded contact relationship between the ribs and the soil is adopted. The model (length \times width \times height) is 12, 6, 7.8m. The soil and ribs parameters in the model are based on the actual material of the intercity railway. The model established using the finite element software is shown in Figure 5 (a).

By comparing the static model with the experimental results, the rationality of the material and contact relationship can be verified. Furthermore, the dynamic model can be used to calculate the soil pressure during high-speed train operation.

In the dynamic model, relevant parameters such as subgrade and foundation are selected according to the actual parameters in relevant literature (Zhai, 2007), while parameters related to dynamic models such as tracks and trains are selected according to the provisions in literature (TB 10025-2019; Li, et al. 2020). Hertz contact relationship is used between vehicle and tracks.

In the model, fixed boundary conditions are set at the bottom of the wall, and displacement boundaries are applied in the longitudinal and transverse directions of the model. A binding contact relationship is adopted between the track bed and the subgrade, and displacement boundary conditions are also set at the longitudinal ends of the rail. The three-dimensional coupling system of vehicle track MSE wall subgrade is shown in Figure 5(b).

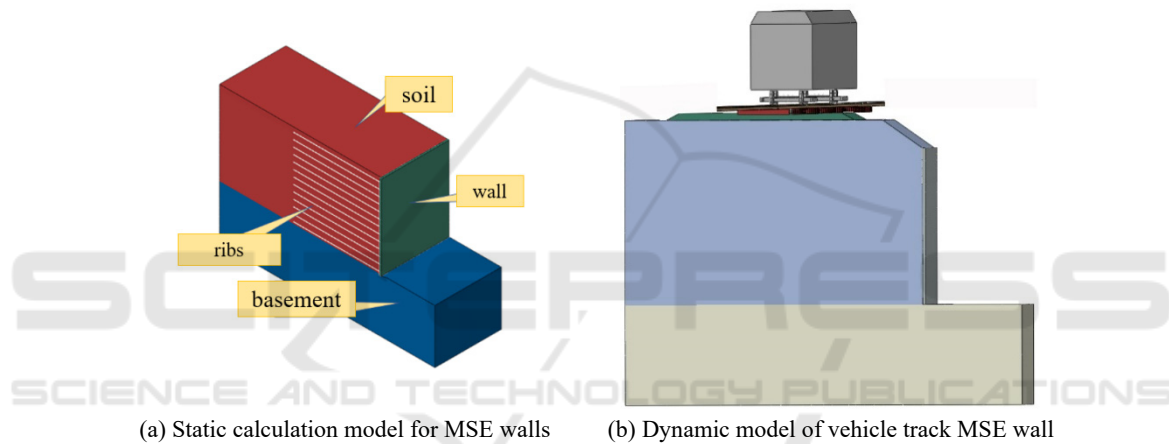


Figure 5: Dynamic calculation model of MSE wall for high-speed railway.

4.2 Model Validation

In the static calculation model, the same load as the test is taken as 10kPa, 20kPa, 30kPa, 40kPa, 50kPa, and 54.1kPa, respectively. The vertical soil pressure cloud map under static loading is shown in Figure 6 (a), and the comparison between the vertical soil pressure at the top of the retaining wall and the test results is shown in Figure 6 (b).

In the calculation, the same load as the test is taken as 10kPa, 20kPa, 30kPa, 40kPa, 50kPa, and 54.1kPa, respectively. The vertical soil pressure cloud map of the MSE wall under static loading is shown in Figure 6 (a), and the comparison between the vertical soil pressure at the top of the wall and the test results is shown in Figure 6 (b).

From Figure 7 (a), it can be seen that at around 0.3 seconds, the first bogie of the train passes through the middle of the wall, and at around 0.6 seconds, the

second bogie of the train passes through the middle of the wall. When the train bogie passes through the wall, there are two obvious peaks in the vertical soil pressure. Compared with static soil pressure, the dynamic soil pressure under the action of a train has a clear variation with time. At the same time, when the train pass through the wall, the soil pressure inside the wall reaches its maximum.

From Figure 7 (b), it can be concluded that under the high-speed trains load, the distribution of soil pressure inside the wall shows a non-linear distribution in the active zone and a linear distribution in the stable zone. The soil pressure in the stable zone is consistent with the law calculated by the Coulomb soil pressure calculation formula. The distribution of soil pressure under train load is only the same as that under static load in the stable zone, but different in the active zone. Therefore, it is recommended to comprehensively consider the effects of dynamic and static loads when calculation.

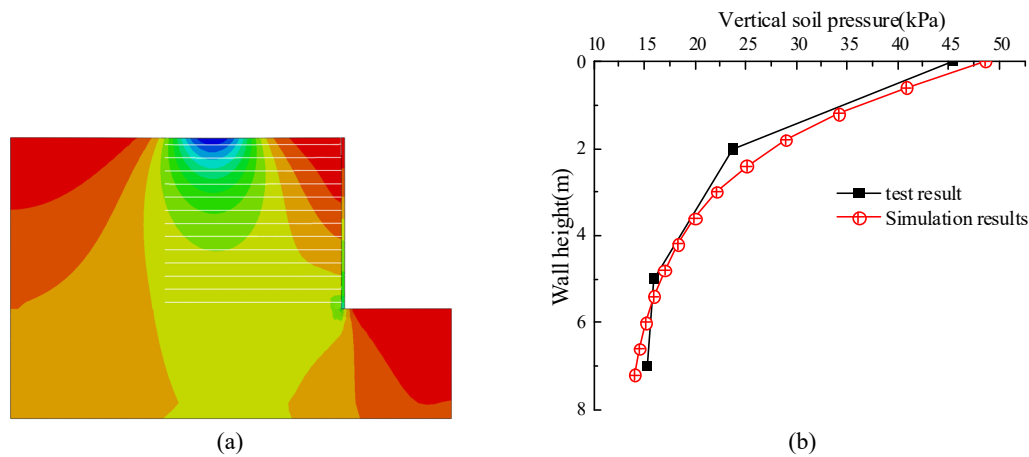


Figure 6: Comparison of vertical displacement.

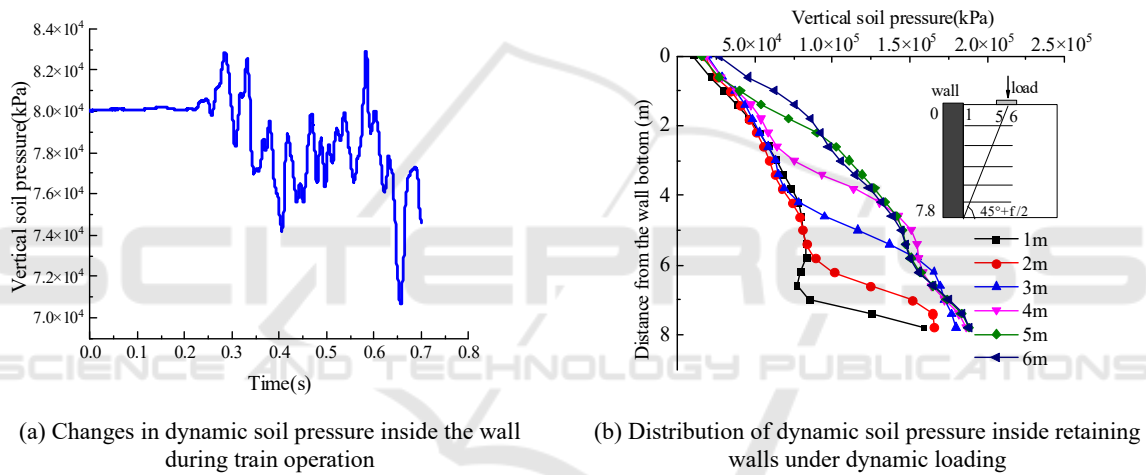


Figure 7: Vertical soil pressure inside the wall under dynamic load.

4.3 Failure of Ribs Leads to Changes in the Soil Pressure Zone and Fracture Surface

When the intercity railway train runs at a speed of 250km/h, the variation of soil pressure at the middle position of the wall with the train running time is shown in Figure 7 (a), and the distribution of soil pressure inside the wall is shown in Figure 7 (b)

It is generally believed that the location of the fracture surface of MSE walls will not change, and the stable and active areas of soil pressure distribution are also unchanged. However, in practical situations, if a layer of ribs in the MSE wall fails, will the regional range change, and how will the corresponding fracture surface change? To study this problem, the following different working conditions were

calculated separately.

(1) Firstly, the stress-strain and fracture surface changes were calculated under the condition of no failure of the reinforcement within the entire range, as follows:

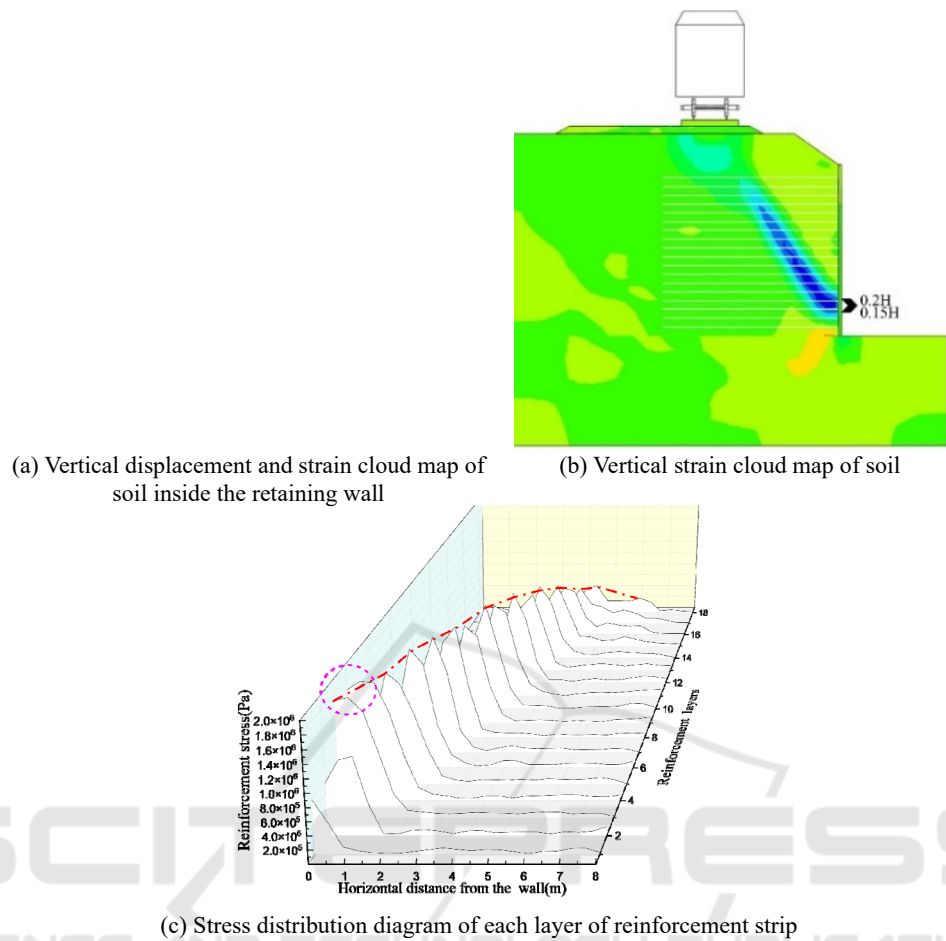


Figure 8: Stress distribution of soil and reinforcement strips when the train passes through the retaining wall.

From Figure 8 (a), it can be observed that when the train passes through the wall, there are two obvious areas of vertical soil displacement inside the wall, one is the inclined downward displacement area, and the other is the inclined upward area at the bottom of the wall. When the train passes through the wall, a shear slip zone will inevitably appear between the two zones. The position the sliding band is $0.15H$ at the bottom of the wall.

From Figure 8 (b), it can be seen that when the train passes through the wall, a significant strain concentrated shear slip zone appears in the soil, with the maximum strain concentrated between $0.15H$ and $0.2H$ at the bottom end.

From Figure 8 (c), it can be obtained that when the train passes through the wall, each layer of ribs shows a significant peak. The location of the fracture surface of the wall is determined by connecting the maximum stress of each layer of ribs with a red line. It can be observed that the maximum stress in the third and fourth layers of the red circle is significantly higher than the others, so the most likely to fracture first is

the third and fourth layers.

It can be seen that the maximum reinforcement stress of the 3rd and 4th layers plays a crucial role in the entire ribs layer. In order to study how the stress distribution of the ribs when two or more layers of ribs fail, and the changes of the shear slip zone and fracture surface inside the wall, the stress and soil strain changes of the ribs were studied when the 3rd, 4th, 5th, and 6th layers fail respectively.

(2) When the third layer of ribs fails, the stress distribution of the ribs inside the retaining wall is shown in Figure 9.

From Figure 9, it can be got that when the third layer ribs fail, the maximum stress of the fourth layer ribs is significantly higher than that of the other layers, and the maximum stress increases by 54% compared to the maximum stress without failure. At the same time, the position of the fracture surface has also undergone significant changes, from the original position of the third layer to the fourth layer, as shown by the red line.

(3) When the fourth layer of ribs fails, the vertical

displacement, strain, and stress distribution of the soil are shown in Figure 10.

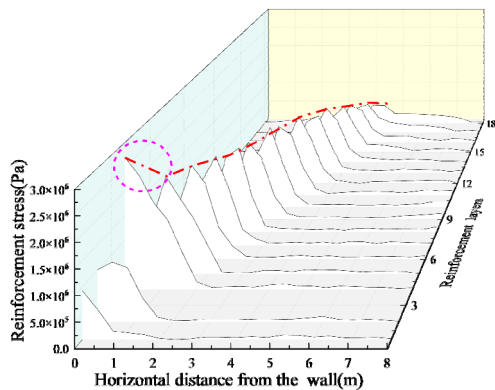
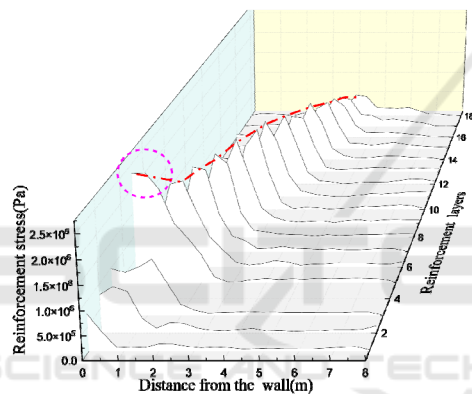


Figure 9: Stress distribution of the ribs in the wall during the third layer fail.



Stress distribution of reinforcement when the fourth layer of reinforcement fails

Figure 10: Stress distribution of soil and reinforcement when the fourth reinforcement fails.

From Figure 10, it can be seen that when the train passes through the wall, there are two obvious areas of vertical dynamic displacement of the soil inside the wall. When the train passes through the retaining wall, a shear slip zone will inevitably appear between the two displacement zones. The position at the bottom of the sliding band is 0.2H from the bottom of the wall.

From Figure 10, it can be seen that when the train passes through the wall, there is a clear sliding slip zone with concentrated strain inside the wall, and the maximum strain is concentrated between 0.2H and 0.25H at the bottom end.

From Figure 10, it can be seen that when the fourth layer's ribs fail, the maximum stress of the fifth ribs is significantly higher than that of the other layers, and the maximum stress increases by 39.7% compared to the maximum stress when without failure. At the same

time, the position of the fracture surface has also undergone significant changes, from the third layer to the fifth layer, as shown by the red line.

Draw the fracture surface positions of the 3rd, 4th, 5th, and 6th layers of the reinforcement ribs when they fail and all layers have no failure in the same diagram. At the same time, the Rankine fracture surface and the railway standard 0.3H fracture surface are also compared and analyzed in the figure, as shown in Figure 11.

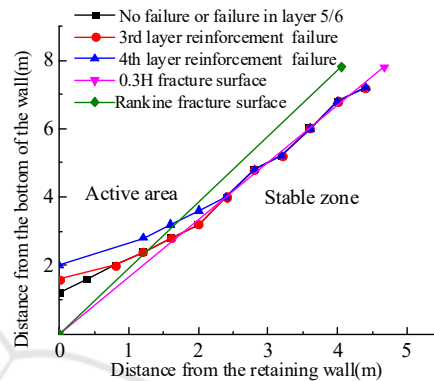


Figure 11: Comparison of fracture surfaces under different layers of reinforcement failure.

From the Figure 11, it can be concluded that when the third layer of ribs fails, the fracture surface of the MSE wall will rise from the original 0.15H to 0.2H. When the fourth layer's ribs fails, the position of the fracture surface will rise from the original 0.15H to 0.25H. When the fifth or sixth layer's ribs fail, the fracture surface returns to the original 0.15H position. It can be seen that only when the ribs fail within the range of 0.15H to 0.25H, the position of the fracture surface inside the MSE wall will change.

By comparing the location of the fracture surface calculated in this article with the American Rankine fracture surface and the 0.3H fracture surface, it can be concluded that the traditional belief is that the location of the fracture surface is fixed and unchanging, and the active and stable areas divided by the fracture surface are also fixed and unchanging. But if the ribs in the range of 0.15H to 0.25H fails, it will change. At the same time, the calculation results of the Rankine fracture surface are relatively small, while the results of the 0.3H fracture surface are relatively conservative.

In the designing of MSE walls for high-speed railways, the ribs at the bottom of the wall should be strengthened within the range of 0.15H to 0.25H. The design principle should ensure that the failure of a

certain layer's ribs will not cause further failure when the stress of the previous layer's increases.

5 CONCLUSION

Model tests were conducted to investigate the soil pressure changes inside MSE walls under static and dynamic train loads. A three-dimensional coupled model of high-speed train track MSE walls was established, and the soil pressure changes and fracture surface were analyzed. The conclusions are as follows:

(1) Through static load tests, it has been found that reducing the spacing and increasing the length of ribs have a certain effect on reducing the soil pressure.

(2) Under static load, the soil pressure is linearly distributed along the depth of the wall. However, under train load, the soil pressure inside the wall is linearly distributed in the stable zone, but exhibits nonlinear trend in the active zone. Therefore, when calculating the soil pressure of the MSE wall, the effects of train and static loads should be comprehensively considered.

(3) In existing designs, it is generally believed that the location of the fracture surface in the active and stable areas of the MSE wall is fixed and unchanged. However, when the ribs at the bottom of the wall fails within the range of $0.15H$ to $0.25H$ under the load of high-speed trains, the fracture surface of the wall will move upwards along the wall. Therefore, in the design of high-speed railway MSE walls, it is recommended to strengthen the designing of the ribs at the bottom of the retaining wall within the range of $0.15H$ to $0.25H$.

ACKNOWLEDGMENTS

This research was funded by the Guangzhou Construction Group Technology Plan Project (Grant no. [2022]-KJ005, [2023]-KJ013, [2023]-KJ014, [2024]-KJ043, [2024]-KJ106, [2024]-KJ105)

REFERENCES

- Jiang, Z. W., Guo, X. Y., Li, W. T., et al. 2016. Self-shrinkage behaviors of waste paper fiber reinforced cement paste considering its self-curing effect at early-ages. *International Journal of Polymer Science*, 2016: 1-12.
- Noike, T., Goo, I. S., Matsumoto, H., et al. 2004. Development of a new type of anaerobic digestion process equipped with the function of nitrogen removal. *Water Science & Technology*, 49(5/6): 173-179.
- Jean, B. P., Alain, C., Emmanuel, B., et al. 2015. Dynamic behavior of a mechanically stabilized earth wall under harmonic loading: experimental characterization and 3D finite elements model. *Computers and Geotechnics*, 65: 199-211.
- Alain, C., Emmanuel, B., Jean, B. P., et al. 2017. Numerical simulation of the response of a reinforced wall to a high speed train passage. *International Journal for Numerical and Analytical Methods in Geomechanics*, 41(11): 1285-1303.
- Fei, S., Liu, H. B., Ma, L. Q., et al. 2018. Numerical analysis of geocell-reinforced retaining wall failure modes. *Geotextiles and Geomembranes*, 46(03): 284-296.
- Ehsan, S. H., Ahoo, A. 2018. Numerical simulation of two-tier geosynthetic reinforced soil walls using two phase approach. *Computers and Geotechnics*, 100:15-29.
- Mohammad, R. S., Jie, H., Sazzad, B. S., et al. 2018. Study of the behavior of mechanically stabilized earth (MSE) walls subjected to differential settlements. *Geotextiles and Geomembranes*, 46(01): 77-90.
- Xiao, C. Z., Li, G. Q., Gao, S., et al. 2021. Dynamic response of tiered geogrid-reinforced soil retaining walls under traffic loading. *Chinese Journal of Geotechnical Engineering*, 43(10): 1789-1797+1961.
- Wang, J. Q., Zhong, W. T., Huang, S. B., et al. 2023. Experimental study on static and dynamic performances of modular reinforced earth retaining wall. *Rock and Soil Mechanics*, 44(05): 1435-1444.
- Ren, F. F., Xu, H., Huang, Q. Q. 2021. Study on deformation and failure mechanisms of reinforced soil retaining walls subjected to horizontal static/dynamic loading. *Chinese Journal of Rock Mechanics and Engineering*, 40(06): 1248-1257.
- Xu, P., Zhong, Y., Ma, H. D., et al. 2023. Upper bound analysis of bearing capacity of reinforced soil retaining walls under strip footing load. *Journal of Railway Engineering Society*, 40(03): 14-19.
- Yang, G. Q., Niu, X. D., Zhou, S. G., et al. 2021. Experimental study on structural behavior of reinforced retaining wall with composite full-height rigid facing. *Rock and Soil Mechanics*, 42(07): 1794-1802.
- Du, Y. X., Liu, H., Zhou, F. 2018. Mechanical properties of hybrid reinforced soil retaining wall. *Journal of Central South University (Science and Technology)*, 49(04): 940-948.
- National Railway Administration Code for Design of High Speed Railway: *TB 10621-2014*. Beijing: China Railway Publishing House, 2014.
- Yang, Y. T. 2015. *The research on engineering properties of QingRong intercity railway reinforced earth retaining wall*. ShijiaZhuang TieDao University. College of Civil Engineering, pp. 31-52.
- Zhai, W. M. 2007. *Vehicle-Track Coupling Dynamics*. 3rd ed. Science Press, Beijing, pp. 390-400.
- National Railway Administration. *Code for design on retaining structures of railway subgrade: TB 10025-2019*. China Railway Publishing House, Beijing. 2019.

Li, L., Zheng, J. J., Cao, W. Z., et al. 2020. Numerical analysis of widening subgrade using pile-supported reinforced-earth wall considering rheological characteristics of subsoil. *Journal of Civil and Environmental Engineering*, 42(02): 65-72.

